(Received 3 July 2023, Accepted 4 November 2023, Scheduled 6 February 2024)

# An Array of Double-Cornu Spiral Antenna

Paul Tcheg[1], Matthias Möck[2], and David Pouhè[3]

[1]Pilz GmbH & Co. KG, Germany
[2]Karlsruhe Institute of Technology, Germany
[3]Reutlingen University of Applied Sciences, Germany

**ABSTRACT:** Based on a framework recently published, the double-Cornu spiral antenna is extended to an array to enhance the gain. The designed array of $2 \times 2$-elements is of low profile and small sizes, has however a large effective bandwidth, and shows overall good radiation characteristics: enhanced gain, large axial ratio bandwidth, and high degree of polarization purity. Except for a few deviations, which are due to manufacturing tolerances, artificial noise and measurement uncertainties on the one hand and diffracted waves at external edges on the other, simulated results and experimental data fit well together. In addition, EMC along with signal integrity issues related to the reduction of noise and unwanted radiation have been addressed. The proposed antenna is suitable for 5G applications and radar systems. With 14.02 dB realized gain, 6.2 GHz effective bandwidth and an uplink data rate of 3.44 Mbit/s, the array is promising for many mobility applications.

## 1. INTRODUCTION

In a recent publication, a new family of planar spiral antennas composed of two Cornu-Spirals rotated by an angle of $\pm\pi/2$ about the axis perpendicular to the antenna plane was presented [1]. A sequential rotation technique was applied to obtain circular polarization. It was shown that the double-cornu spiral antenna (DCSA) does not need to fear comparison with other antennas of the same size in the literature [2–5], as it has good radiation characteristics.

Although the DCSA is of high gain (max. gain 9.3 dBi), its use as a single antenna in some ubiquitous systems is limited, especially in applications where high-gain directive antennas are needed. To overcome this drawback, an array configuration to enhance the gain is required.

This work addresses this issue. It presents an array of $2 \times 2$-elements of DSCA as shown in Section 2.

The array uses the DSCA as a single element; therefore, details on the design of the DSCA will not be reproduced here in order not to inflate the work unnecessarily. Readers seeking the design procedure of the DCSA are referred to [1]. However, proper due is given to manufacturing requirements [6] for production purposes during the design of each antenna array as for the DCSA.

The proof of the pudding being in the eating, predicted data are always compared to measurements throughout the whole work (Section 3). Possible applications in non-terrestrial communications for automotive are proposed in Section 4. The work ends with some concluding remarks (Section 5).

* Corresponding author: David Pouhè (david.pouhe@reutlingen-university.de).

## 2. DESIGN OF THE ANTENNA ARRAY

### 2.1. Array Configuration

To find out the best arrangement of array elements, a parameter study of two potential array configurations, the square and star configurations, (Fig. 1) has been carried out. The two configurations are obtained from the DCSA. The first one, *viz* star configuration, is obtained through an easily arrangement of the radiating elements by successively applying the matrix translation $Tv_1$

$$T_{v_1} = \begin{bmatrix} 0 \\ d_y \\ 0 \end{bmatrix} \tag{1}$$

to obtain two array elements (eight radiating elements) where $d_y$ is the distance between two adjacent array elements in the $y$ direction and the matrix translation $T_{v_2}$

$$T_{v_2} = \begin{bmatrix} d_x \\ 0 \\ 0 \end{bmatrix} \tag{2}$$

to get the two remaining array elements. In (2) $d_x$ is the distance between two adjacent array elements in the $x$ direction. The relative position of the radiating elements to the substrate edges is $\lambda_{eff}/4$ at 24 GHz. However, the star-configuration exhibits a relatively large space inside the array, increasing with the spacing between array elements. It may lead to destructive interference of radiated field from array elements and impact the whole array's radiation properties. Therefore, an alternative array configuration is called for, and it was designed while considering the compactness of the final antenna.

**TABLE 1**. Comparison between the star-array and square configuration by variation of distance $d$.

| Parameter | $d = \lambda/8$ | | $d = \lambda/4$ | | $d = \lambda/2$ | |
|---|---|---|---|---|---|---|
| | Star | Square | Star | Square | Star | Square |
| Gain at 24 GHz, ($\vartheta = 0°$) | 14.80 dB | 13.99 dB | 14.87 dB | 14.17 dB | 14.94 dB | 15.21 dB |
| ABW at 24 GHz, $\varphi = 0°$ | $[-16°; +16°]$ | $[-17°; +17.5°]$ | $[-16°; +16°]$ | $[-17°; +17°]$ | $[-17°; +16°]$ | $[-25°; +25°]$ |
| SLL at 24 GHz, $\varphi = 0°$ & 90° | −10.07 dB | −13.9 dB | −8.96 dB | −12.7 dB | −7.57 dB | −13.1 dB |

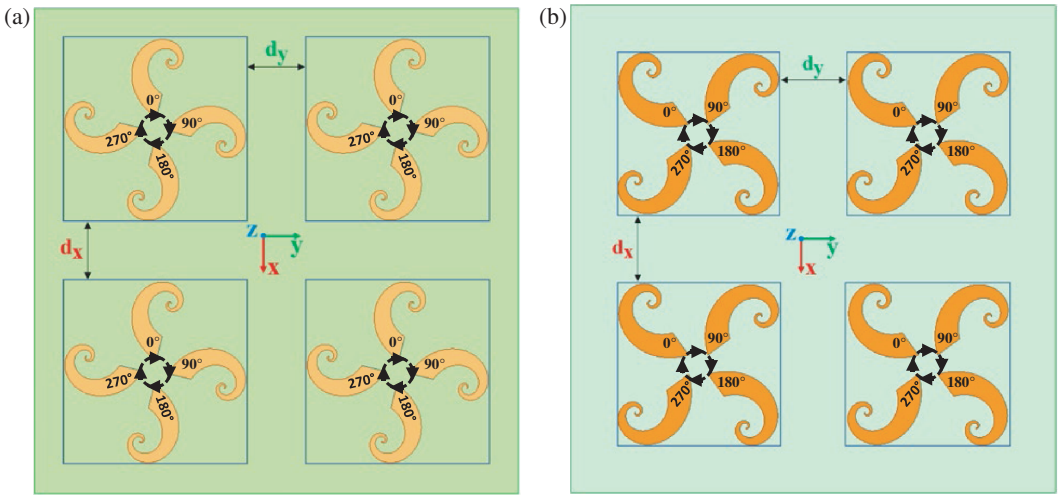


**FIGURE 1**. (a) Star and (b) square configuration of the 2 × 2-array of DCSA with the illustration of the sense of the sequential rotation.

The alternative option is realized by rotating the core elements by 50° around the axis perpendicular to the antenna plane and using (1) and (2) as implemented for the star-array configuration. Fig. 1 shows the alternative configuration, and it is named in the following the square-array configuration.

A comparative study on the performance of the two configurations was performed. It was found that the square configuration performed favorably compared to the star one as can be seen from observation of Table 1. It was therefore decided to pursuit investigations with the square configuration (Fig. 1(b)), whereby $d_x = d_y = d = \lambda/2$. Other distances $d$ between the elements may be possible; however, $d = \lambda/2$ (at 24 GHz) is the distance with the lowest side lobe level (SLL) (Table 1).

### 2.2. The Feeding Network

The feeding network (Fig. 2(a)) uses the feed of the single DCSA as the essential building block of the array feed. Recall that the DCSA is fed using an integrated wideband stripline sequential phase power network (SPPN) as described in [1]. Four SPPNs are arranged under the area of radiating elements to efficiently utilize the space allocated to the feed design. The impedance of the input line is adjusted from 50 Ω to 100 Ω corresponding to a trace width of 108.8 µm in the SPPNs. Then, the impedance of the transformation trace (quarter-wavelength) required is 40.2 Ω with a corresponding width of 684 µm. To minimize signal integrity (SI) issues, particularly EM coupling between two traces, top and bottom SPPNs are arranged such that their input lines are combined through a Y-junction towards the input port at the edge of the PCB. The then obtained network was further optimized by performing a parametric sweep on geometrical parameters building a single SPPN and adding shorting pins close to the input port to stabilize the line impedance while analyzing the overall performances of the feeding network.

Figures 2(b), 2(c), and 2(d) show the reflection coefficient at the input, insertion, and phase difference between the output ports. The designed feeding network has an impedance bandwidth of 17.47 GHz, from 11.1 GHz to 28.57 GHz. At operation frequency (24 GHz), the insertion loss (IL) diagrams depict values with an acceptable deviation ranging from −12.13 dB to −13.89 dB. The desired value of IL at each output port of SPPN, −12.04 dB, remains an ideal value, as material losses of the PCB should be considered. In addition, the impact of unsuppressed unwanted modes (propagating in the PCB) on the frequency response of the SPPN network should also be considered. Distortion-free frequency responses up to 31 GHz can be observed in IL and phase diagrams. The phase difference varies between +1 and −1.4° at 24 GHz from the ideal value 90°. This variation is due to the interferences in the cavity, deteriorating the phase at each port. Feed enlargement may also play a role here. Table 2 summarizes simulation results of the feeding network array.

Signal vias with a diameter of 250 µm are modeled to connect spirals and the feed network applying the methodology pre-

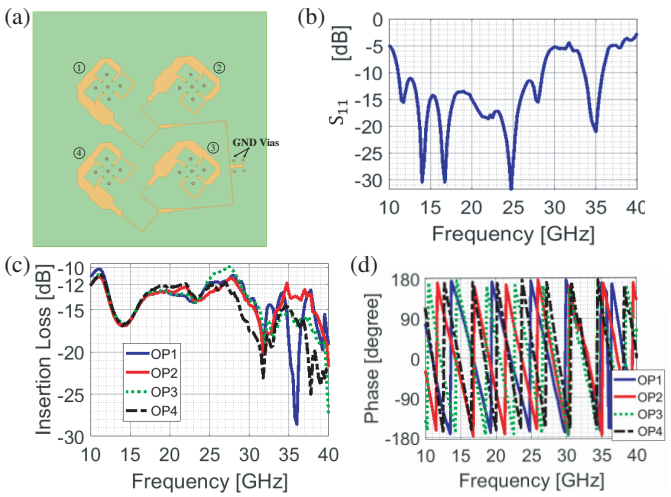


**FIGURE 2**. (a) Feeding network, (b) reflection coefficient, (c) insertion loss at outputs of the SPPN and (d) phase of the feeding network. OP stands for output port. All results are simulated.

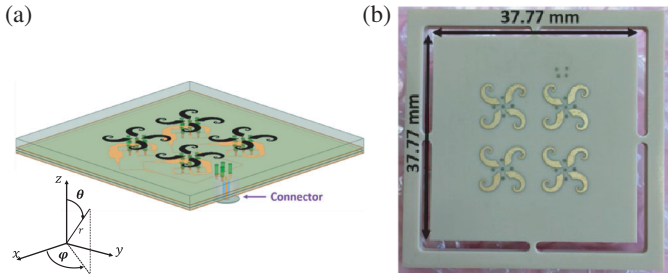


**FIGURE 3**. The 3D simulation model of (a) the fabricated $2 \times 2$ DCSA array, (b) prototype.

sented in [7] and considering the manufacturing requirements and, a k-connector soldered on the feed's GND as depicted in Fig. 3.

## 3. RESULTS AND DISCUSSION

The designed antenna according to Fig. 3 is square with overall dimension 37.77 mm $\times$37.77 mm $\times$2.41 mm. It was simulated using Ansys-HFSS Electronics Desktop 19.0, manufactured and tested in self-made anechoic chamber.

Figures 4 to 9 display the obtained simulated radiation characteristics. For comparison, measured data have been added. Experimental data were obtained throughout this work using

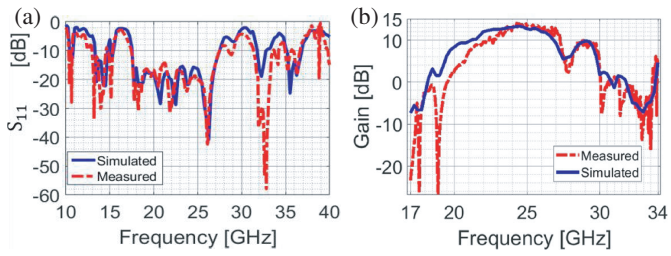


**FIGURE 4**. (a) Measured and simulated reflection coefficient and (b) gain of the fabricated $2 \times 2$ DCSA array.

**TABLE 2**. Summary of simulated feeding network data.

| Parameter | SPPN 1 | SPPN 2 | SPPN 3 | SPPN 4 |
|---|---|---|---|---|
| RL Bandwidth ($S_{in,in}$) | 17.47 GHz from 11.1 GHz to 28.57 GHz | | | |
| Parameters at 24 GHz | | | | |
| $S_{in,in}$ | $-21.13$ dB | | | |
| $S_{1,in}$ | $-13.23$ dB | $-12.48$ dB | $-12.13$ dB | $-12.65$ dB |
| $S_{2,in}$ | $-13.81$ dB | $-13.89$ dB | $-12.80$ dB | $-13.19$ dB |
| $S_{3,in}$ | $-13.13$ dB | $-12.41$ dB | $-12.13$ dB | $-12.43$ dB |
| $S_{4,in}$ | $-13.13$ dB | $-12.43$ dB | $-12.37$ dB | $-12.67$ dB |
| $\varphi_{S_{2,in}} - \varphi_{S_{1,in}}$ | 90.3° | 90° | 90.4° | 89.3° |
| $\varphi_{S_{3,in}} - \varphi_{S_{2,in}}$ | 90.3° | 90.4° | 89.4° | 90.5° |
| $\varphi_{S_{4,in}} - \varphi_{S_{3,in}}$ | 88.6° | 90° | 90° | 90.5° |
| $\varphi_{S_{1,in}} - \varphi_{S_{4,in}}$ | 91.1° | 89.6° | 90.2° | 90° |

an in-house made far-field antenna measurement system consisting of a full-anechoic chamber operating from 3 to 80 GHz, a linearly polarized standard gain horn antenna, with a constant gain of 13 dB from 17 to 34 GHz, and a network analyzer (R$\alpha$S ZNB) [1]. The measurement step was 50.0 MHz for frequencies and 5° for the elevation angle.

The fabricated DCSA array has an overall impedance bandwidth of over 14.5 GHz, divided into three windows from 17.44 GHz to 27.47 GHz, from 31.5 GHz to 34.2 GHz, and from 35 GHz to 37 GHz. The simulated reflection coefficient bandwidth exceeding 13 GHz ranges from 17.52 GHz to 27.5 GHz, from 31.5 GHz to 32.5 GHz, and a narrow window from 35 GHz to 37 GHz. The shape of both plots matches very well over the analysis band. Between 14.5 GHz and 17.5 GHz the antenna shows high impedance values due to reflections at the connection point between the coaxial connector and the stripline on the one hand, and other interactions between the center conductor and the edge of the stripline ground plane on the other hand.

At the operation frequency and for $\varphi = 0°$, the fabricated antenna radiates a circularly polarized field at the broadside and in the angle window ranging from $-26°$ to $+17°$ and the simulated band spanning from $-19°$ to $+18°$. As shown in Fig. 6(a), measured and simulated angular bandwidth (ABW) plots are in good agreement, indicating that the connector interface was efficiently modeled. In addition to artificial noise and measurement uncertainties, the discrepancy between the results of both structures is undoubtedly caused by the connector interface and the slight extension of the PCB for this purpose. These two aspects change the configuration of the wave propagation at the feed's input, causing spurious radiation to superpose the incident circularly radiation, inversing its sense and consequently degrading the desired polarization at some elevation angles.

From 21.5 GHz to 27 GHz, the gain obtained from simulation is at least 10 dB, while for measurement, it is the case from 22 GHz to 27.45 GHz. The maximum gain is recorded at 24.5 GHz for simulation and is 13.3 dB. In contrast, the measured peak gain is 14.02 dB at 24.3 GHz. Despite the frequency shift of about 0.8 GHz attributed to the parasite capacitances and inductances around the connector interface and unavoidable fabrication and measurement errors, the measured gain along the operation frequency window corroborates the simulated one (Fig. 4(b)). An average increase in gain of 5 dB over the band of interest can be noted compared to that of the single DCSA.

Figure 5(b) depicts the axial ratio (AR)'s measured and simulated results as a function of the frequency. One can see that experimental results corroborate data obtained from the simulated model over the analysis band, where the overall measured effective bandwidth (EBW) is 6.2 GHz, and the simulated one is 6.6 GHz. The discrepancies observed around 22 GHz are due to the fabrication tolerances regarding the connector soldering. Furthermore, it was observed that the connector-fed array exhibits a broadened AR about 1 GHz compared to the AR of the fabricated single DCSA [1]. However, it is worth mentioning that the 3-dB bandwidth of the array of DCSA at the broadside and all azimuth angles is very similar to that of the single DCSA [1].

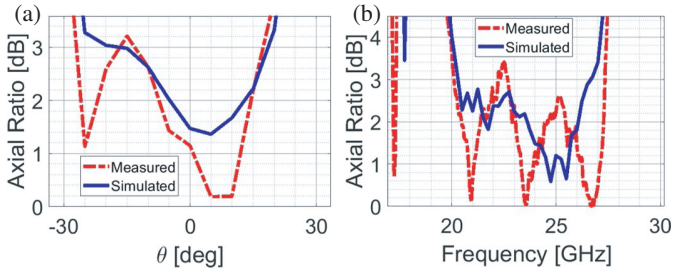


**FIGURE 5**. Measured and simulated axial ratio of the fabricated $2 \times 2$ DCSA array. (a) Versus the elevation angle at 24 GHz and for $\varphi = 0°$ and (b) over the frequency at $\vartheta = 0°$ and $\varphi = 0°$.

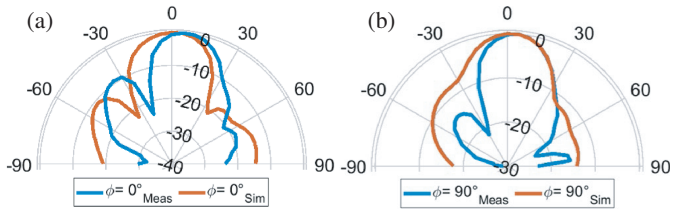


**FIGURE 6**. Measured and simulated axial radiation pattern at 24 GHz of the fabricated $2 \times 2$ DCSA array. (a) $\varphi = 0°$ and (b) $\varphi = 90°$.

Comparisons of measured and simulated radiation patterns at three frequencies (24 GHz, 25 GHz, and 26 GHz) included in the EBW and in the frequency range in which the gain is higher than or equal to 10 dB are portrayed in Figs. 6 to 9. The antenna array still radiates the M1 mode over a large frequency range. Despite a few discrepancies caused by manufacturing tolerances regarding the soldering of the pin connector and inaccuracies during measurement, the consistency between simulation and experiments can be appreciated by comparing obtained results. At almost all frequencies and in both cut-planes $\varphi = 0°$ and 90°, the 3-dB beamwidth of the simulated pattern varies between 25° and 30°, while the measured HPBW fluctuates between 20° and 30°. At the operation frequency, the measured SLL varies between −10 dB and −18 dB for cut-planes $\varphi = 0°$ and is −15 dB for $\varphi = 90°$ while the simulated SLL is between −10.5 dB and −14 dB for cut-planes $\varphi = 0°$. In contrast, at 25 GHz, simulated SLL is about −12 dB independent of considered cut-plane while measured SLL values of −22 dB, 19.1 dB, −17 dB, and −12 dB are recorded respectively for $\varphi = 0°$ and $\varphi = 90°$. The measured SLL value at 26 GHz lies between −10 dB and −15 dB, while the simulated one is between −10 dB and −14 dB.

An asymmetry is observed in all patterns regardless of the cut plane, and it is more pronounced in the measured patterns. Leading causes for this asymmetry and all discrepancies between experimental and simulated data are, amongst others, the

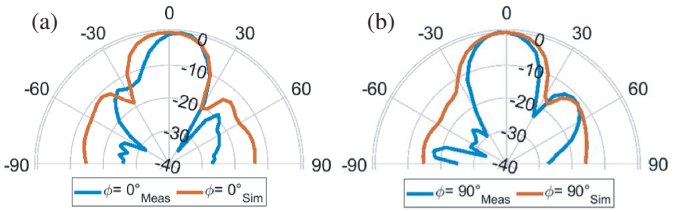


**FIGURE 7**. Measured and simulated axial radiation pattern at 25 GHz of the fabricated $2 \times 2$ DCSA array. (a) $\varphi = 0°$ and (b) $\varphi = 90°$.

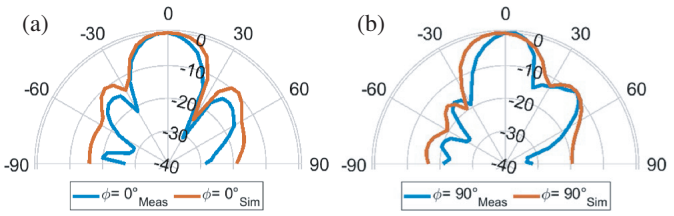


**FIGURE 8**. Measured and simulated axial radiation pattern at 26 GHz of the fabricated $2 \times 2$ DCSA array. (a) $\varphi = 0°$ and (b) $\varphi = 90°$.

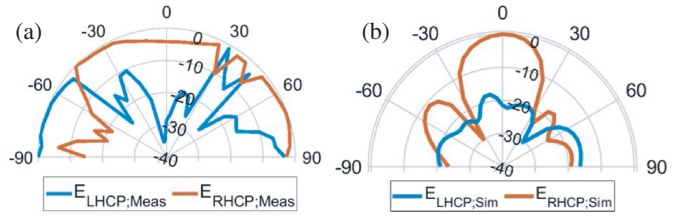


**FIGURE 9**. Co- and cross-polarization patterns at $\varphi = 0°$ and 24 GHz. (a) Measured and (b) simulated.

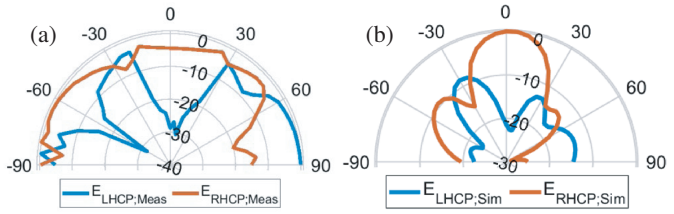


**FIGURE 10**. Co- and cross-polarization patterns at $\varphi = 90°$ and 24 GHz. (a) Measured and (b) simulated.

**TABLE 3**. Performance comparison with some existing antennas in the literature.

| Antenna type and Ref. | Wideband stack [11] | A Ka-Band High-Gain [9] | Low-Profile Circularly [10] | 2 × 2 Slot Spiral Cavity [12] | This work |
|---|---|---|---|---|---|
| **Technology** | Microstrip/ Dual-layer | Microstrip + Sequential rotation | SIW + Sequential rotation | Printed gap waveguide + Sequential rotation* | Stripline + Sequential rotation |
| **Structure** | 2-layers | Single-layer | 2-layers | 4-layers | 3-layers |
| **Typ of Element** | Patch + parasitic circular-patch sequential rotation | Patch | Cavity-backed slot | Slot spiral | Patch spiral |
| **Feed Location** | Layer under radiating elements | Same layer with radiating elements | under slot/ substrate | Layer under radiating elements | Layer under radiating elements |
| **Dimensions [mm]** | $11 \times 11 \times 1.62$ | $16 \times 16 \times 0.254$ | $38.5 \times 38.5 \times 1.07$ | $22.9 \times 22.9 \times 2.028$ | $37.77 \times 37.77 \times 2.45$ |
| **Operation Frequency [GHz]** | 30 | 29 | 28 | 38 | 24 |
| **Impedance BW [GHz]** | 7.5 | 4.59 | 6.35 | 5.76 (simulated) | 14.73 |
| **ABW at op. freq.** | - | - | - | - | $[-26°; +17°]$ |
| **Peak Gain at boresight [dB]** | 12.2 at 30 GHz | 13.59 at 29.3 GHz | 8.65 at 27.9 GHz | 10.15 at 36 GHz | 14.02 at 24.3 GHz |
| **SLL at op. frequency** | $-15$ dB ($\varphi = 0°$) $-12$ dB ($\varphi = 90°$) | $-18$ dB ($\varphi = 0°$); $-18$ dB ($\varphi = 90°$) | $-10$ dB and $-7$ dB at ($\varphi = 90°$) | $-10$ dB ($\varphi = 0°$); $-10$ dB ($\varphi = 90°$) both at 39 GHz | $-10$ dB ($\varphi = 0°$); $-15$ dB ($\varphi = 90°$) |
| **Cross-Polarization Level at the zenith and op. freq.** | 32 dB ($\varphi = 0°$); 24 dB ($\varphi = 90°$) | - | - | 15 dB ($\varphi = 0°$); 18 dB ($\varphi = 90°$) both at 39 GHz | 27 dB ($\varphi = 0°$); 27 dB ($\varphi = 90°$) |

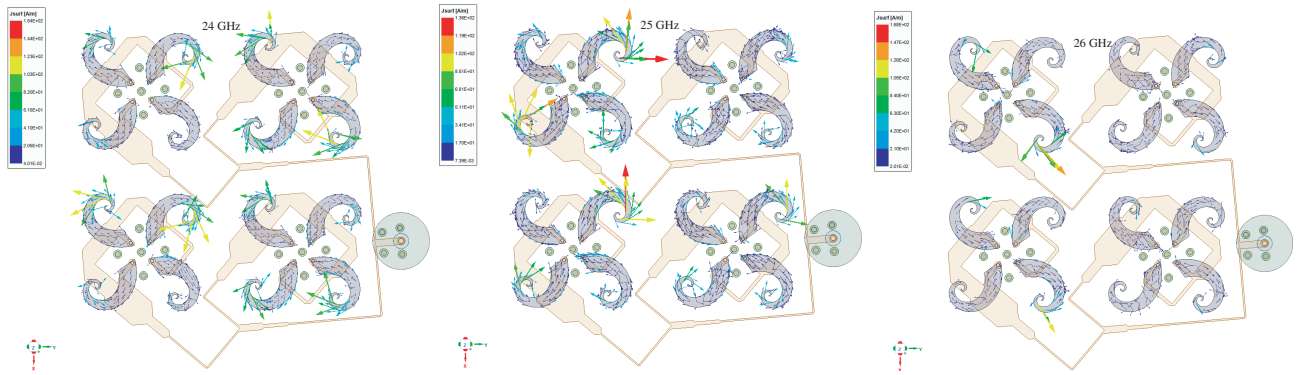


**FIGURE 11**. Current distribution at 24 GHz, 25 GHz and 26 GHz for 0° phase.

enlargement of the PCB to mount the k-connector, the inductive effects of the soldered pin at higher frequencies, as well as unavoidable errors during measurements. In addition, the asymmetry observed in the measured patterns compared to the simulated ones is partially due to the phase center deviation. Because the fabricated antenna is not an ideal point of source, and the phase center cannot be related to its geometrical center for the entire frequency band, the phase difference varies depending on the observation point. Note that the phase center of the measurement horn antenna was not determined during the antenna alignment process.

It was also observed during simulation that the antenna is very sensitive to any variation in parameter values. In fact, a small change in either the radii of the shorting pins, the probe position and its displacement or the position and the size of the shorting posts, caused dramatic change in the antenna behavior.

**TABLE 4**. Link Budget Calculation (Uplink).

| Parameter | Value |
|---|---|
| Frequency of operation ($f$) | 24.3 GHz |
| Orbital height ($d$) | 400 km |
| Max Output Power ($P_{UE}$) | 28 dBm |
| UE Antenna gain ($G_{UE}$) | 14.02 dBi |
| Atmospheric Effects ($AT_{losses}$) | 12.5 dBi |
| LEO Sattelite Antenna Gain ($G_{sat}$) | 44.3 dBi |
| LEO Noise Figure ($NF$) | 3 dB |
| Signal Bandwidth ($B$) | 5 MHz |

| Parameter | Formula | Value |
|---|---|---|
| Free Space Path Loss (FSPL) | $92.44 + 20 \cdot \log_{10}(d_{\text{km}}) + 20 \cdot \log_{10}(f_{\text{GHz}})$ | 172.19 dB |
| Effective Isotropic Radiated Power (EIRP) | $P_{UE} + G_{UE}$ | 42.02 dBm |
| Received Power at LEO Satellite ($P_{rec_{sat}}$) | $EIRP - FSPL - AT_{losses} + G_{sat}$ | $-98.37$ dBm |
| SNR at Demodulator ($SNR_{dem}$) | $P_{resat} - NF - [-173 + 10 \cdot \log_{10}(1000000 \cdot B)]$ | 4.64 dB |
| Efficiency | $0.1769 \cdot SNR_{dem} - 0.132$ | 0.688 Bits/s/Hz |
| Maximum Data Rate | *Effeciency* $\cdot B$ | 3.44 Mbit/s |

**TABLE 5**. Link Budget Calculation (Downlink).

| Parameter | Value |
|---|---|
| Frequency of operation ($f$) | 24.3 GHz |
| Orbital height ($d$) | 400 km |
| Satellite Output Power per Channel ($P_{sat}$) | 45 dBm |
| UE Antenna gain ($G_{sat}$) | 14.02 dBi |
| Atmospheric Effects ($AT_{losses}$) | 12.5 dBi |
| LEO Sattelite Antenna Gain ($G_{sat}$) | 44.3 dBi |
| UE Noise Figure ($NF$) | 3 dB |
| Signal Bandwidth ($B$) | 40 MHz |

| Parameter | Formula | Value |
|---|---|---|
| Free Space Path Loss (FSPL) | $92.44 + 20 \cdot \log_{10}(d_{\text{km}}) + 20 \cdot \log_{10}(f_{\text{GHz}})$ | 172.19 dB |
| Effective Isotropic Radiated Power (EIRP) | $P_{sat} + G_{sat}$ | 89.3 dBm |
| Received Power at UE Antenna ($P_{rec_{UE}}$) | $EIRP - FSPL - AT_{losses} + G_{UE}$ | $-81.37$ dBm |
| SNR at Demodulator ($SNR_{dem}$) | $P_{reUE} - NF_{UE} - [-173 + 10 \cdot \log_{10}(1000000 \cdot B)]$ | 12.60 dB |
| Efficiency | $0.1769 \cdot SNR_{dem} - 0.132$ | 2.09 Bits/s/Hz |
| Maximum Data Rate | *Effeciency* $\cdot B$ | 83.94 Mbit/s |

This notwithstanding, it can be seen that the overall behaviors of predicted and measured data match well.

Figures 9 and 10 show measured and simulated co- and cross-polarizations at 24 GHz and for planes $\varphi = 0°$ and $\varphi = 90$. Similar trends between experiments and simulation results can be observed despite the undesired fluctuations in measured patterns due to measurement errors but also to diffracted fields at the external edges. Guide- and surface-waves excited within the waveguide made up of the two conducting planes (top and bottom metal layers) and the substrates surrounding the feeding network propagate along the line and radiate as diffracted waves at the external edges. These fields not only generate distortion of the antenna radiation characteristics such as gain reduction, pattern asymmetry, impedance variation, and reduction of the axial ratio bandwidth but also impact the cross-polarization performance of the antenna [8].

As the single DCSA, the array is right hand circularly (RHC) polarized with relatively high polarization purity. In the bore-

sight direction, the measured cross-polarization level is about $-27$ dB in both cut planes, while the simulated one is $-22$ dB for $\varphi = 0°$ and $-21$ dB for $\varphi = 90$. Furthermore, Figs. 9 and 10 confirm the polarization purity obtained in Fig. 5(a), in which experimented and simulated ABWs for $\varphi = 0°$ were compared.

Representative for all frequencies, Fig. 11 displays the current distribution on radiating elements at 24 GHz, 25 GHz, and 26 GHz. As the frequency varies, the sense of the current also changes.

Performance comparison of the proposed antenna array and that of existing antennas of the same sizes (or nearly) in the literature is presented in Table 3. As can be seen the DSCA array does not need to fear any comparison; it performs favorably.

## 4. POSSIBLE APPLICATIONS

To find out possible application scenarios, link budget calculations were performed for satellite communication for 5G-automotive [13]. Applying well-known link budget approaches [14] and taking into consideration parameters presented in Tables 4 and 5-left, link budget calculations based on the realized gain show that the proposed DCSA-array can transmit data rate up to 3.44 Mbit/s in uplink and receive 83.94 Mbit/s in downlink in non-terrestrial communication with an orbital height of 400 km (LEO). High data rates are achievable by taking high signal bandwidth into consideration according to specific requirement.

Based on predicted data, which may be transmitted in the uplink scenario, the antenna can be used for the following applications in 5G automotive communication: tele-operated driving, accident report, high definition map collecting and sharing, infrastructure assisted environment perception.

## 5. CONCLUSION

The newly presented family of spiral antenna, the DCSA, has been extended to a $2 \times 2$-element array. The antenna is as expected of high gain, has a large effective bandwidth, and has a high degree of polarization purity. In spite of the unwanted asymmetry in the radiation patterns due to edge diffraction and other interactions within the device, good characteristics are recorded over the frequency band of interest, thus making the antenna a good candidate for 5G and radar applications. Simulated and experimental data show good agreement. The array is promising for many mobility applications with 14.02 dB realized gain, 6.2 GHz effective bandwidth, and an uplink data rate of 3.44 Mbit/s.

Electromagnetic compatibility (EMC) and signal integrity issues related to noise reduction and unwanted radiation have been addressed.

Although developing the $2 \times 2$ DCSA-array only for M1 mode radiation was intended, it is possible to realize the conical mode by designing an appropriate feeding network.

The $2 \times 2$-array presented here can be used as a subarray to obtain large arrays which may be used as phased arrays or MIMO antennas, as will be shown in coming works.

## REFERENCES


[1] Tcheg, P., M. Möck, and D. Pouhè, "A new broadband antenna of high gain: the double-cornu spiral antenna," *Progress In Electromagnetics Research C*, Vol. 118, 199–212, 2022.

[2] Chen, H., Y. Shao, Y. Zhang, C. Zhang, and Z. Zhang, "A low-profile broadband circularly polarized mmWave antenna with special-shaped ring slot," *IEEE Antennas and Wireless Propagation Letters*, Vol. 18, No. 7, 1492–1496, Jul. 2019.

[3] Mener, S., R. Gillard, and L. Roy, "A dual-band dual-circular polarization antenna for Ka-band satellite communications," *IEEE Antennas and Wireless Propagation Letters*, Vol. 16, 274–277, 2017.

[4] Nasimuddin, X. Qing, and Z. N. Chen, "A wideband circularly polarized microstrip array antenna at Ka-band," *2016 10th European Conference on Antennas and Propagation (EuCAP)*, Davos, Switzerland, 2016.

[5] Liu, W., W. Chen, and A. Zhang, "Design of a wideband stack array antenna for Ka-band satellite communication application," *2021 IEEE 4th International Conference on Electronic Information and Communication Technology (ICEICT)*, 345–348, Xi'an, China, 2021.

[6] http://www.contag.de/uploads/pi_ti/technische_ausfuehrung.pdf.

[7] Tcheg, P. and D. Pouhè, "A design methodology for the implementation of planar spiral antennas with an integrated corporate feed," *Progress In Electromagnetics Research C*, Vol. 106, 239–253, 2020.

[8] Salazar, J. L., N. Aboserwal, J. D. Diaz, J. A. Ortiz, and C. Fulton, "Edge diffractions impact on the cross polarization performance of active phased array antennas," *2016 IEEE International Symposium on Phased Array Systems and Technology (PAST)*, 1–5, MA, USA, 2016, doi: 10.1109/ARRAY.2016.7832571.

[9] Chen, A., Y. Zhang, Z. Chen, and S. Cao, "A Ka-band high-gain circularly polarized microstrip antenna array," *IEEE Antennas and Wireless Propagation Letters*, Vol. 9, 1115–1118, Nov. 2010.

[10] Wu, Q., H. Wang, C. Yu, and W. Hong, "Low-profile circularly polarized cavity-backed antennas using SIW techniques," *IEEE Transactions on Antennas and Propagation*, Vol. 64, No. 7, 2832–2839, Jul. 2016, doi: 10.1109/TAP.2016.2560940.

[11] Liu, W., W. Chen, and A. Zhang, "Design of a wideband stack array antenna for Ka-band satellite communication application," *2021 IEEE 4th International Conference on Electronic Information and Communication Technology (ICEICT)*, 345–348, Xi'an, China, 2021, doi: 10.1109/ICEICT53123.2021.9531139.

[12] Baghernia, E., M. M. M. Ali, and A. R. Sebak, "$2 \times 2$ slot spiral cavity-backed antenna array fed by printed gap waveguide," *IEEE Access*, Vol. 8, 170609–170617, 2020, doi: 10.1109/ACCESS.2020.3024564.

[13] Tayyab, U., H.-P. Petry, A. Kumar, Md. G. Robbani, T. Wack, and M. A. Hein, "Link budget and design approach of a non-terrestrial 5G automotive antenna," *Proc. of the 52nd European Microwave Conference*, 864–867, Milan, Italia, Sept. 27–29, 2022.

[14] Singh, K., A. V. Nirmal, and S. V. Sharma, "Link margin for wireless radio communication link," *ICTACT Journal on Communication Technology*, Vol. 08, No. 03, 1574–1581, Sept. 2017, htt://doi: 10.21917/ijct.2017.0232.